Available online at www.sciencedirect.com
SCIENCE DIRECT
Icarus 182 (2006) 143–160
ICARUS
www.elsevier.com/locate/icarus

Photometric analysis of 1 Ceres and surface mapping from HST observations

Jian-Yang Li [a,*], Lucy A. McFadden [a], Joel Wm. Parker [b], Eliot F. Young [b], S. Alan Stern [b], Peter C. Thomas [c], Christopher T. Russell [d], Mark V. Sykes [e]

[a] *Department of Astronomy, University of Maryland, College Park, MD 20742, USA*
[b] *Department of Space Studies, Southwest Research Institute, 1050 Walnut Street, Boulder, CO 80302, USA*
[c] *Center for Radiophysics and Space Research, Cornell University, Ithaca, NY 14853, USA*
[d] *IGPP & ESS, University of California Los Angeles, Los Angeles, CA 90095, USA*
[e] *Planetary Science Institute, 1700 East Fort Lowell, Tucson, AZ 85719, USA*

Received 4 May 2005; revised 12 December 2005

Available online 2 February 2006

Abstract

The highest resolution (pixel scale 30 km) images of Ceres to date have been acquired by the Advanced Camera for Surveys onboard Hubble Space Telescope, through three wide band filters, centered at 535, 335, and 223 nm, covering more than one rotation of Ceres. The lightcurve at 535 nm agrees with earlier observations at V-band [Tedesco, E.F., Taylor, R.C., Drummond, J., Harwood, D., Nickoloff, I., Scaltriti, F., Schober, H. J., Zappala, V., 1983. Icarus 54, 23–29] in terms of magnitude, amplitude, and shape. The 0.04 magnitude lightcurve amplitude cannot be matched by Ceres' rotationally symmetric shape, and is modeled here by albedo patterns. The geometric albedos at the above three wavelengths are measured to be 0.087 ± 0.003, 0.056 ± 0.002, and 0.039 ± 0.003, respectively. V-band geometric albedo is calculated to be 0.090 ± 0.003, consistent with earlier observations [Tedesco, E.F., 1989. In: Binzel, R.P., Gehrels, T., Matthews, M.S. (Eds.), Asteroids II. Univ. of Arizona Press, Tucson, pp. 1090–1138]. A strong absorption band (30%) centered at about 280 nm is observed, but cannot be identified with either laboratory UV spectra or the spectra of Europa or Ganymede. The single-scattering albedo has been modeled to be 0.070 ± 0.002, 0.046 ± 0.002, and 0.032 ± 0.003, respectively. The photometric roughness of Ceres' surface is found to be about $44° \pm 5°$ from photometric modeling using Hapke's theory, consistent with earlier radar observations [Mitchell, D.L., Ostro, S.J., Hudson, R.S., Rosema, K.D., Campbell, D.B., Velez, R., Chandler, J. F., Shapiro, I.I., Giorgini, J.D., Yeomans, D.K., 1996. Icarus 124, 113–133]. The first spatially resolved surface albedo maps of Ceres at three wavelengths have been constructed from HST observations, as well as the corresponding color maps. Eleven surface albedo features are identified, ranging in scale from 40–350 km. Overall the range of these albedo and color variations is small compared to other asteroids and some icy satellites.

Keywords: Asteroids; Photometry; Surfaces

1. Introduction

Unlike small asteroids, which are probably the products of disruptive collisions, the largest main-belt asteroids are protoplanets that were too large to be shattered and dispersed. Their growth to full sized terrestrial planets was choked off when the asteroid belt was depleted in mass due to the rapid formation of Jupiter early in the history of the Solar System. Among small bodies, of particular importance are those near the expected distance where water is marginally stable, and starts to condense to liquid or solid ice (Watson et al., 1963), thus where the innermost icy bodies form. Current observational evidence shows that the boundary between rocky bodies and icy bodies is probably somewhere within the asteroid belt or a little further from the Sun. The composition of the inner main-belt asteroids is more silicate-rich, while some outer main-belt asteroids contain hydrated silicates (Bell et al., 1989, and references therein). Further small bodies such as the satellites of giant planets are rich in ice.

The first asteroid discovered in 1801, Asteroid 1 Ceres, is the largest of these planetary embryos, and is located in the

* Corresponding author.
E-mail address: jyli@astro.umd.edu (J.-Y. Li).

0019-1035/$ – see front matter
doi:10.1016/j.icarus.2005.12.012

main asteroid belt with a semi-major axis 2.77 AU, close to the water condensation boundary. Despite its relatively large apparent angular size as observed from the Earth, little is known about Ceres' composition, current evolutionary status, or history, because of the difficulty in interpreting its reflectance spectrum, and the failure to find any spectral matches from available meteorite samples (Chapman and Salisbury, 1973; Johnson and Fanale, 1973). The shape and size of Ceres have been determined from earlier observations to be an oblate spheroid (Millis et al., 1987; Parker et al., 2002; Drummond et al., 1998; Saint-Pé et al., 1993), with an effective radius ranging from 471 to 489 km. The mass is measured by observing the perturbations of Ceres on other asteroids, and has been estimated to be 9.4×10^{20} kg (Viateau and Rapaport, 1998; Michalak, 2000; Standish, 2001, JPL interoffice memorandum 312, F-01-006 dated April 11). The visual geometric albedo of Ceres is reported to be 0.073 (Millis et al., 1987), and 0.10±0.01 (Tedesco, 1989), higher than the albedo of carbonaceous chondrite material (3–5%), which at one time was considered to be the main compositional material of Ceres (Johnson and Fanale, 1973).

NASA has selected the Dawn mission to orbit Ceres (starting in 2013) and Vesta (starting in 2008) to investigate its role in the early evolution of terrestrial planets, and to characterize the conditions and processes of the Solar System's earliest epoch (Russell et al., 2004).

2. HST observations

In support of this mission, we observed Ceres with Hubble Space Telescope (HST) through the High Resolution Channel of the Advanced Camera for Surveys (ACS/HRC) over more than one complete rotation (Table 1). The observations were carried out before its opposition in December 2003, and after in January 2004. Three wide band filters, F555W, F330W, and F220W, centered at 535, 335, and 223 nm, respectively, were used to cover the expected strong absorption in Ceres' spectrum at UV. The pixel scale is about 30 km during our observations, corresponding to about 3.5° longitude/latitude at the equator. The heliocentric distance (r) and geocentric distance (Δ) were 2.6 and 1.6 AU, respectively. The phase angles (α) range from 5.4° to 7.4°.

From these HST observations, Thomas et al. (2005) have precisely determined the size, shape, and polar orientation of Ceres. By fitting the limbs of imaged disks with ellipses as it is rotating, Thomas et al. (2005) determined that Ceres has an oblate spheroidal shape within an uncertainty of about 2 km, with an equatorial radius of 487.3 ± 1.8 km and a polar radius of 454.7 ± 1.6 km. Its shape and smooth limb indicate that it is a gravitationally relaxed body. The rotation has been constrained by the orientation of its short axis, and by tracking the motion of a bright spot on the surface as well. The north pole was determined to be at RA = 291° and Dec = 59° (J2000), within 5° uncertainty. From the best determined mean density, 2077 ± 36 kg m^{-3}, as calculated from its volume and earlier mass measurement, Thomas et al. (2005) concluded that, Ceres is more likely to be differentiated with a rocky core surrounded by an ice mantle, rather than homogeneous as concluded earlier (Millis et al., 1987). The water fraction of Ceres was estimated from its mean density, the densities of common materials in large asteroids, and a simple differentiated internal structure model, to be from 16 to 26%, a reasonable value for objects at the solar distance of Ceres (Wilson et al., 1999; Grimm and McSween, 1989). McCord and Sotin (2005) modeled Ceres' thermal evolution with finite difference spherically symmetric models. Constrained by the size, density and composition, they predict changes in the dimensions of Ceres over the age of the Solar System that should have manifestations on the surface in terms of tectonic features and disruptions at the surface. In the analysis presented here, we explore the photometric properties of Ceres at spatial scales of 30 km as a preliminary look at the surface of Ceres prior to the Dawn mission.

Table 1
The aspect data of the HST observations. Three filters F555W, F330W, and F220W were used for all three runs

UTC date and time	r[a] (AU)	Δ[b] (AU)	α[c] (°)	# of images
28-Dec-2003 10:51:59 to 28-Dec-2003 19:36:48	2.611	1.653	6.2	192
30-Dec-2003 15:39:49 to 30-Dec-2003 16:23:56	2.609	1.645	5.4	25
23-Jan-2004 23:34:12 to 24-Jan-2004 03:30:16	2.595	1.648	7.4	50

[a] Heliocentric distance.
[b] Earth range.
[c] Phase angle.

3. HST data reduction

The HST images are calibrated to an absolute photometric scale, both reduced magnitude with heliocentric distance r and Earth range Δ at 1 AU, and the standard reflectance unit I/F, where I is the intensity detected by HST, and πF is the incident solar flux received at the surface of Ceres.

The HST images were processed through the standard reduction pipeline, which applies CCD related corrections, bad-pixel removal, bias correction, dark correction, and flat field (Pavlovsky et al., 2005). We then applied geometric distortion corrections, and rotated the images to north-up. Cosmic rays cannot be removed with the traditional method of combining multiple exposures because Ceres is rotating very fast. They are dealt with later. Photometric calibration was done in two steps. First, all images were calibrated to reduced magnitude at $r = 1$ AU and $\Delta = 1$ AU. Then they were converted to reflectance units I/F. The detailed procedures for photometric calibration are described in Appendix A.1.

The absolute photometric calibration of ACS/HRC images should be generally better than 2% (Pavlovsky et al., 2004), which we take as the absolute photometric uncertainty for F555W images. Considering the uncertainties of the high resolution solar spectra we used to calibrate images from F330W filter, and the throughput characteristics of ACS imaging system (see Appendix A.1 for details), we estimated 3% as the absolute photometric uncertainty for this set of images. The uncertainty of absolute photometry for filter F220W is greater because these images have a significant red leak. Red leak correction

can be relatively accurate for stars with known colors or spectral types (Pavlovsky et al., 2004). However, with insufficient information about the color of Ceres at visible wavelengths through UV, the correction can only be estimated with a relatively high uncertainty. Our treatment for red leak is described in Appendix A.1 as a part of the photometric calibration. The absolute photometric uncertainty for F220W images is estimated to be 8%.

Another possible source of uncertainty for both absolute photometric calibration and relative photometry across the disk of Ceres comes from the imperfect charge transfer efficiency (CTE) of ACS/HRC CCD (Pavlovsky et al., 2004). It is estimated that the uncertainty caused by CTE is much less than 1% for absolute photometry, and about 4×10^{-4} across the disk of Ceres. Therefore we ignored the contribution of CTE to photometric uncertainty.

4. Disk-integrated photometry

4.1. Lightcurve and geometric albedo

The total reduced magnitude of Ceres, $M(1, 1, \alpha)$, at 6.2° solar phase angle plotted vs sub-Earth longitude is shown in Fig. 1. The average magnitude of Ceres, $M(1, 1, \alpha)$, through F555W filter is 3.87 ± 0.02 mag, 3.92 ± 0.02 mag, and 3.97 ± 0.02 mag at solar phase angles 5.4°, 6.2°, and 7.4°, respectively. Because of the flat spectrum of Ceres at wavelengths longer than 400 nm, the 0.04 mag correction to convert solar magnitude from standard Johnson V-band filter to F555W filter (Pavlovsky et al., 2004) is still valid for Ceres, yielding V magnitudes of Ceres 3.83 mag, 3.88 mag, and 3.93 mag at the above three solar phase angles we observed, respectively. These fall on the phase curve obtained by Tedesco et al. (1983) nicely. The shape and the amplitude of the lightcurve through F555W filter agrees with earlier ground based observations at V-band at similar phase angles (Tedesco et al., 1983; Taylor et al., 1976; Schober, 1976; Gehrels and Owings, 1962; Ahmad, 1954). The 0.04 mag lightcurve amplitude, which is roughly 4% of the average brightness, although small compared to the lightcurve amplitudes of other asteroids, cannot be produced by Ceres' rotationally symmetric shape (Thomas et al., 2005). The only explanation is that the surface of Ceres shows some non-randomly distributed albedo patterns.

From the total brightnesses at three wavelengths, the geometric albedo can be calculated by

$$p(\lambda) = \frac{r^2 \Delta^2}{R_{\text{Ceres}}^2} \frac{F_{\text{Ceres}}(\lambda, \alpha)}{F_{\odot}(\lambda)} f(\alpha), \quad (1)$$

where r and Δ are the heliocentric (in AU) and geocentric (in km) distances of Ceres. R_{Ceres} is the equivalent radius, which we used 470.7 km, the geometric mean of the two axes of its best fit oblate spheroidal shape model (Thomas et al., 2005). $F_{\text{Ceres}}(\lambda, \alpha)$ is the measured total flux of Ceres at solar phase angle α, through each filter. $F_{\odot}(\lambda)$ is solar flux at 1 AU through the same filter. From the IAU-adopted HG phase system (Bowell et al., 1989) with a slope parameter $G = 0.12$ for Ceres (Lagerkvist and Magnusson, 1990), the phase correction factor $f(\alpha)$ is calculated to be 1.54, 1.60, and 1.69 for solar phase angles 5.4°, 6.2°, and 7.4°. The absolute magnitude, $M(1, 1, 0)$, of Ceres at V-band is calculated to be 3.36 ± 0.02 mag, consistent with its H parameter of 3.38 ± 0.02 as reported by Lagerkvist and Magnusson (1990). The geometric albedo of Ceres as measured through three filters, F555W, F330W, and F220W, are calculated to be 0.087 ± 0.003, 0.056 ± 0.002, and 0.039 ± 0.003, respectively, assuming the same phase function as in V-band. With the 0.04 mag correction applied to the geometric albedo measured through F555W filter, the V-band geometric albedo of Ceres is 0.090 ± 0.003. This value is consistent with the geometric albedo of 0.10 ± 0.01 as measured from IRAS observations (Tedesco, 1989), but different by about 23% from the value reported by Millis et al. (1987), which used the mean absolute V-band magnitude of 3.61 ± 0.03 as reported by Tedesco et al. (1983) in the calculation. Further investigation finds that the absolute V-band magnitude reported by Tedesco et al. (1983) was obtained by extrapolating a linear phase law fitted from the observations at phase angles higher than 7°. The phase curve of Ceres shows an obvious opposition surge that is not accounted for by a linear phase law, but has been taken care

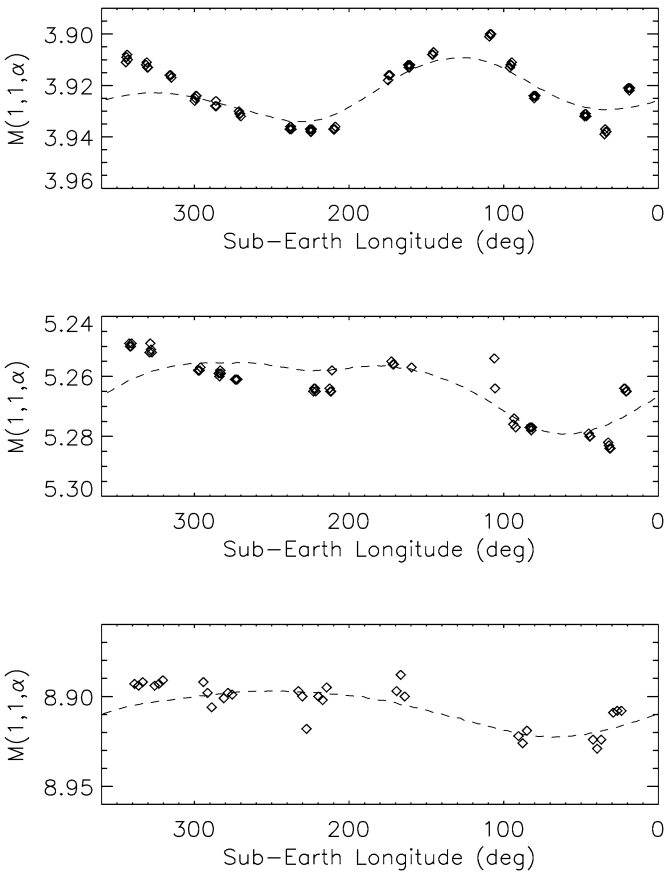

Fig. 1. The lightcurves of Ceres are plotted in symbols for F555W filter (upper panel), F330W filter (middle panel) and F220W filter (lower panel), as functions of sub-Earth longitude. The synthetic lightcurves constructed from our SSA maps are plotted as dashed lines (Section 5.4). The absolute photometric uncertainties are about 2% (0.022 mag) for F555W images, 3% (0.032 mag) for F330W images, and 8% (0.084 mag) for F220W images. Relative uncertainties between images are better than 1% (0.011 mag).

of by the G-parameter of the HG phase system as reported by Lagerkvist and Magnusson (1990). The opposition amplitude of about 0.25 mag as shown in Fig. 3 of Tedesco et al. (1983) completely explains the 23% difference between the geometric albedo reported by Millis et al. (1987) and ours to within error bars.

4.2. Spectrum

The HST observations provide the reflectance of Ceres at three wavelengths, complementing earlier measurements (Parker et al., 2002; Chapman and Gaffey, 1979). Fig. 2 shows the spectrum at visible wavelengths from the 24-color asteroid survey rescaled such that the geometric albedo of Ceres as measured through our F555W data roughly agrees with the 24-color spectrum by interpolation. The most prominent feature is a strong absorption band centered at about 280 nm, with a full width at half maximum (FWHM) of about 120 nm, and about 30% reflectance relative to V-band. With the large uncertainty of the geometric albedo at 162 nm from Parker et al. (2002), the blue side of the band is not well defined. But the existence of an absorption band is consistent with the different mechanisms for the absorption features as discussed by Gaffey et al. (1989).

The Hartley band of O_3 (290 nm vicinity) falls in the wavelength region of our analysis. We consider the possibility that this spectral feature is contaminated by terrestrial, atmospheric ozone. Further analysis (see Appendix A.2) shows that all HST images are free of ozone contamination from terrestrial atmosphere. For our observations, the spectral feature is indeed from the surface of Ceres.

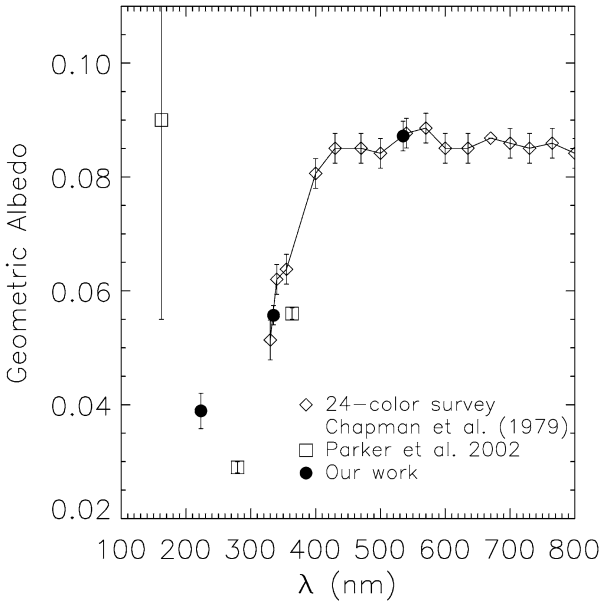

Fig. 2. The spectrum of Ceres constructed from our measurement and earlier observations. Plotted as y-axis is the geometric albedo at various wavelengths. One point at 670 nm from 24-color surveys does not have uncertainty estimate available. No relevant discussions about red leak for points from Parker et al. (2002) are found from the literature. The uncertainties for our measurements are about 2% for 535 nm, 3% for 335 nm, and 8% for 223 nm, respectively.

Spectral absorption bands at similar wavelengths have been detected for Jupiter's icy satellites, Europa and Ganymede. A broad absorption feature in the UV spectrum of Europa was first noted by Lane et al. (1981), and confirmed by Noll et al. (1995). It was attributed to an SO band, caused by the implantation of sulfur ions from Jupiter's magnetosphere into the water-ice surface on the trailing hemisphere (Lane et al., 1981; Sack et al., 1992; Noll et al., 1995). An absorption band at similar wavelength has been observed on Ganymede, but was identified to be the Hartley band of ozone (Noll et al., 1996) on Ganymede. The density ratio of $[O_3]/[O_2]$ on Ganymede has been estimated to be 10 times the peak ratio of the Earth's atmosphere in the same paper. Although the UV absorption band in Ceres' spectrum could also be due to ozone or SO_2 trapped in Ceres' surface, it is much stronger than those in the spectra of Jupiter's satellites. Unlike Europa and Ganymede, Ceres is not in an environment as highly radiative with a continuous supply of sulfur and oxygen as are Europa and Ganymede. We have compared the absorption band with available laboratory measured UV spectra (Wagner et al., 1987) as well, but found that none of them matches the absorption band in both the strength and the wavelength. More observations with higher spectral resolution are needed to characterize the strong UV absorption feature in Ceres' spectrum, and to reveal its nature. In addition, this feature may or may not be correlated with other absorption bands observed for Ceres at longer wavelengths, such as at 600 and 670 nm (Vilas and McFadden, 1992; Vilas et al., 1993), the broad 3 μm band (Lebofsky et al., 1981; Feierberg et al., 1981), and the 3.07 μm band (King et al., 1992).

5. Disk-resolved analysis

With the sunlit disk of Ceres resolved into about 750 pixels, and the precisely determined yet simple shape (Thomas et al., 2005), the normal direction of a surface element imaged in each pixel can be analytically calculated, enabling disk-resolved photometric modeling. The excellent signal-to-noise ratio of greater than 1000 for HST images of Ceres allows us to study its surface reflectance variations, which are expected to be 4% or higher as indicated by its lightcurve.

5.1. Hapke's model

We used Hapke's scattering theory (Hapke, 1993) to model the disk-resolved bidirectional reflectance of the surface of Ceres. The bidirectional reflectance of a rough surface, $r(i, e, \alpha)$, is a function of incidence angle, i, emission angle, e, and phase angle, α,

$$r(i,e,\alpha) = \frac{w}{4\pi}\frac{\mu_{0e}}{\mu_{0e}+\mu_e}\Big\{\big[1+B(\alpha)\big]p(\alpha)-1 + H(\mu_{0e})H(\mu_e)\Big\}S(i,e,\alpha). \quad (2)$$

w is the single scattering albedo (SSA hereafter). μ_{0e} and μ_e are the cosines of the effective incidence angle and emission angle, which are corrected from the true incidence angle and emission angle by the roughness parameter, $\bar{\theta}$, due to the tilt of

the facets within one unresolved unit on a rough surface. The corresponding equations are from Hapke, 1993 (pp. 344). $B(\alpha)$ is the opposition effect correction,

$$B(\alpha; B_0, h) = \frac{B_0}{1 + \frac{1}{h\tan(\alpha/2)}}. \quad (3)$$

Because the opposition effect only affects the brightness of a surface at very small phase angle (usually less than 10°), the two parameters in this part, the amplitude B_0 and width h, can only be determined by photometric data densely sampled at small phase angles. $p(\alpha)$ is the single-particle phase function, which we adopted using the single-term Henyey–Greenstein (HG) form with one parameter, the asymmetry parameter, g,

$$p(\alpha) = \frac{1 - g^2}{(1 + 2g\cos\alpha + g^2)^{3/2}}. \quad (4)$$

$H(\mu_{0e})$ and $H(\mu_e)$ are Chandrasekhar's H function, for which we took the form in Hapke (2002)

$$H(x; w) \approx \left[1 - wx\left(r_0 + \frac{1 - 2r_0x}{2}\ln\frac{1+x}{x}\right)\right]^{-1}, \quad (5)$$

where $r_0 = (1-\gamma)/(1+\gamma)$, and $\gamma = \sqrt{1-w}$. $S(\alpha)$ is a correction term for rough surfaces due to shadows and mutual blocking at non-zero phase angles, parameterized by the roughness parameter, $\bar{\theta}$. It is equal to 1 at opposition. The equations for $S(\alpha; \bar{\theta})$ have been provided by Hapke, 1993 (pp. 344–345).

A least-χ^2 fit was performed. We calculated χ^2's as defined by

$$\chi^2 = \frac{1}{N}\sum_i (r_{i,\text{model}} - r_{i,\text{measure}})^2 \quad (6)$$

for different sets of Hapke's parameters, where N is the number of bidirectional reflectance data points, and $r_{i,\text{model}}$ and $r_{i,\text{measure}}$ are the modeled and measured bidirectional reflectance, respectively. The smallest χ^2 is searched in the grid of parameter space. The parameter set corresponding to the smallest χ^2 is taken as the modeled set of parameters. The percentage square root of χ^2, or root mean square (RMS), relative to the average value, for the modeled parameters was taken as an indicator of the goodness of fit. In addition to Hapke's modeling, we have also used this least-χ^2 searching technique to fit Minnaert model and a modified Minnaert model to Ceres' surface, as discussed in later text.

The HST observations only cover a small range of phase angles (5.4°–7.5°). According to Hapke's photometric model, phase parameters such as the asymmetry factor (g) and opposition parameters (B_0 and h) cannot be reliably determined from the small range of phase angles covered here. Therefore we used those parameters from Helfenstein and Veverka (1989), $g = -0.4$, $B_0 = 1.6$, $h = 0.06$, in our analysis. Only the SSA, w, and the roughness parameter, $\bar{\theta}$ are modeled from our data. On the other hand, since the HST images cover the whole rotation of Ceres, we can construct surface maps. For this purpose, the geometric effects in all images have to be removed with the modeled limb darkening profile. To prevent the uncertainties in phase parameters (g, B_0, and h) from affecting our modeling of limb darkening profile, and in turn generating artifacts in the SSA maps, we decided to only use the images taken in the first HST observing run that are almost at one single phase angle (6.1°–6.2°), so that the phase function term $[1 + B(\alpha)]p(\alpha) - 1 + H(\mu_{0e})H(\mu_e)$ is almost a constant. With the coverage of the whole rotation of Ceres, the average Hapke's parameters of Ceres' surface can be modeled, and the albedo maps can be constructed.

Fitting Hapke's parameters shows that at all three wavelengths, only the central portion of Ceres' disk, with i and e less than about 50° (F555W and F330W) or 40° (F220W), can be well modeled with small residuals of about ±2% and free of any systematic deviation associated with particular incidence and emission angles (Fig. 3). The modeled parameters are listed in Table 2. For the outer annulus, Hapke's model results in large residuals and systematic bias with respect to geometry. Other empirical models, including the Minnaert model, and a modified Minnaert model, are employed to fit the outer annulus, with the model residual shown in Fig. 3, too (see later text). Fig. 4 shows an image of Ceres through F555W filter, and the scan along its photometric equator (the great circle defined by the sub-solar and sub-observer points) and mirror meridian (the great circle where $i = e$), with the fit with Hap-

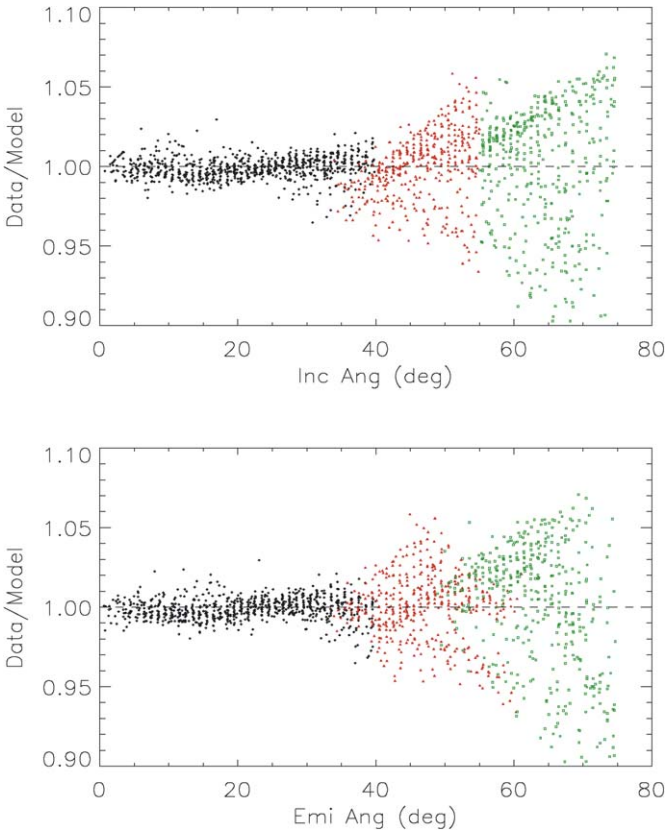

Fig. 3. The ratio of the measured reflectance to modeled reflectance for the HST images through filter F555W, plotted as functions of incidence angle and emission angle. Black dots represent the fit with a Hapke's model, red dots a Minnaert's model, and green dots a modified Minnaert's model (see later text). The scatter for i's and e's in Hapke's modeling is below ±2% level. Similar plots (not shown here) are seen for other two filters.

Table 2
Modeled Hapke's parameters and Minnaert's parameters for the central portion of Ceres' disk

λ (nm)	Number of data points	w[b]	$\bar{\theta}$[c]	RMS (%)	Modeled A_{Geo}[d]	Measured A_{Geo}[a]
			Hapke's model			
535	1088	0.070	48	1.4	0.089	0.087 ± 0.003
335	667	0.046	38	1.1	0.058	0.056 ± 0.002
223	545[e]	0.032	38	1.6	0.041	0.039 ± 0.003
		A[f]	k[g]			
			Minnaert's model			
535	1088	0.092	0.62	0.95		
335	667	0.059	0.58	1.0		
223	545[e]	0.042	0.55	1.6		

[a] The geometric albedo as directly measured from images and corrected for phase function.
[b] Single-scatter albedo from Hapke's modeling.
[c] Roughness parameter from Hapke's modeling.
[d] The modeled geometric albedo from the best-fit Hapke's parameters. For Ceres at the three wavelengths we studied, this value is very close (within 0.5%) to its normal reflectance.
[e] Only data with i and e less than 40° are included in modeling.
[f] Minnaert's albedo from Minnaert's modeling.
[g] Minnaert's limb darkening parameter k.

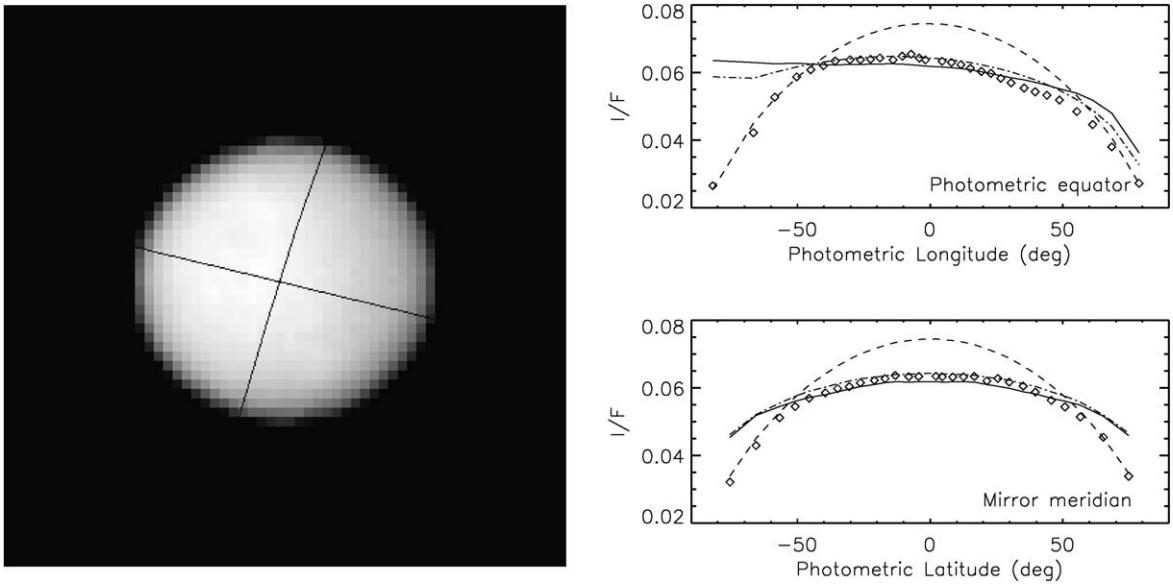

Fig. 4. Left panel shows an image of Ceres through F555W filter. The image is displayed north up. The (nearly) horizontal line marks the photometric equator, and the (nearly) vertical line marks the mirror meridian. In the right panel the scans along the photometric equator and the mirror meridian are plotted, respectively, as symbols. Three models are plotted as lines, with solid line for Hapke's model, dash–dot line for Minnaert's model, and dashed line for the modified Minnaert's model. It is clearly shown that Hapke's model fits the center part of Ceres disk very well, but fails for areas close to limb and terminator. The modified Minnaert's model provides the best fit for areas close to limb and terminator. Similar case applies to images through other two filters.

ke's model, Minnaert model, and the modified Minnaert model, respectively. The SSA through F555W filter is 0.070 ± 0.002, yielding a modeled geometric albedo of 0.089, which corresponds to a modeled V-band geometric albedo of 0.093. The SSA at 335 and 223 nm is determined to be 0.046 ± 0.002, 0.032 ± 0.003, respectively. The modeled geometric albedos at three wavelengths (Table 2) agree with the values directly measured from the images earlier, though slightly higher. The difference is possibly caused by the fact that we only took the center, relatively brighter, region of Ceres' disk in our modeling. The V-band SSA of Ceres is low compared to both mafic silicate-rich asteroids and icy moons of giant planets, but high relative to the most common type of asteroids, C-types, and comets.

The roughness parameter of Ceres is fitted by Hapke's model to be $48° \pm 3°$ from F555W images, $38° \pm 4°$ from F330W images, and $38° \pm 8°$ from F220W images. The uncertainties of those modeled values are estimated as follows. We first calculated the values of I/F for one modeled SSA and the two trial values of roughness that bracket the corresponding modeled roughness at that wavelength. Then we calculated the average difference of I/F for the two roughness values within the region where we used the data to perform photometric modeling (e.g., $i < 50°$ and $e < 50°$ for F555W images) in a

percentage. If the average percentage difference is comparable with or slightly higher than the model residual, then we consider the two corresponding trial values of roughness to define the boundary of the uncertainty range of the modeled roughness. Because surface roughness is a topographical parameter, it should not depend on wavelength, except for very bright surfaces where multiple scattering illuminates shadows to mimic the effect of low roughness. We take the weighed average of the fitted roughness at three wavelengths, $44° \pm 5°$, as our modeled roughness parameter. The formal error of $\pm 5°$ here is calculated following the standard formulae of error propagation.

The high roughness of Ceres is different from the value that Helfenstein and Veverka (1989) adopted (20°) in their modeling with ground-based observations, which could not constrain the roughness because of the limited phase angle and the disk-integrated nature of their data. Whereas the spatial resolution of our data permits constraints on $\bar{\theta}$. Radar observations indicate that Ceres' surface is very rough at scales larger than meters to tens of meters. The radar-detected RMS slope $\theta_{\rm rms}$ of Ceres is 20°–50° (Mitchell et al., 1996), defined as

$$\tan\theta_{\rm rms} \equiv \langle \tan^2\theta \rangle^{1/2} = \left[\int_0^{\pi/2} \tan^2\theta p_P(\theta) \sin\theta \, {\rm d}\theta \right]^{1/2}, \qquad (7)$$

where $p_P(\theta)$ is the slope probability distribution. The RMS slope of Ceres translates to a photometric roughness parameter, $\bar{\theta}$, about the same value. But the polarization characteristics of the same radar echo also indicate that the surface of Ceres is very smooth at centimeter to decimeter scales. Therefore, the high roughness of Ceres refers to the scale between our resolution (tens of kilometers) and centimeter scale.

5.2. Minnaert model

Another commonly used, however empirical, limb darkening model is the Minnaert model (Minnaert, 1941), where the reflectance of a surface is described by $r(i, e) = A \cos^k i \times \cos^{k-1} e$, with a constant A called Minnaert albedo, and a constant k. Usually both Minnaert parameters depend on phase angle (McEwen, 1991). Unlike Hapke's model, Minnaert model does not yield the SSA of the surface. Parker et al. (2002) found that, different from other asteroids and the Moon, Ceres has a very high Minnaert k of about 0.9, meaning a strong brightness drop from disk center towards the limb. However, near-IR observations in H and K bands (1.55–1.80 and 1.95–2.40 μm, respectively) show a flatter brightness profile for the center 60% of the disk, indicating a Minnaert parameter k close to 0.5 (Saint-Pé et al., 1993).

We used Minnaert model to fit Ceres, and found that, at all three wavelengths, Minnaert model yields a good fit in the places where Hapke's model does, and is also good for the immediate outer annulus until i and e about 60°, as shown by the red dots in Fig. 3, but not the outermost annulus of Ceres' disk. For the central portion of the disk, the value of Minnaert parameter is found to be about 0.6 for all three wavelengths (Table 2), a better agreement with the value found from the near-IR observations. Since the phase angle of our observations is 6.2°, which is closer to that of the near-IR observations ($\alpha = 9°$) than to that of Parker et al. (2002) ($\alpha = 19°$), it is very likely that the difference between the modeled k is due to phase angle change. If this is true, then it indicates that the limb darkening properties of Ceres strongly depend on phase angle, but not on wavelength. The phase angle dependence of the Minnaert parameter for Ceres is stronger than that of the icy satellites of Uranus (Veverka et al., 1989). Whether this dependence is due to a geometrical origin or particle's single-scattering properties cannot be determined.

5.3. Modified Minnaert model

In addition to the above models, we also attempted to model the outer rim where either Hapke's model or Minnaert model failed, to see whether the limb darkening can be described by any other model. By observing the bidirectional reflectance as a function of incidence angle and emission angle, we noticed that, for the rim of Ceres' disk where i and e are higher than 50° (40° for images at UV), the reflectance depends on both i and e strongly, but with different dependence. The dependence is not like what is predicted by a Minnaert model with a k parameter close to 1, in which case the reflectance depends on $\cos i$ strongly, while on $\cos e$ rather weakly. Thus we tried a model that introduces one more free parameter from Minnaert model, where

$$r(i, e) = A \cos^k i \cos^j e. \qquad (8)$$

A is a constant, equivalent to Minnaert albedo. k and j are two different power indices, representing different dependence of the reflectance on incidence angle i and emission angle e. If $j = k - 1$, then this model reduces to the Minnaert model.

Least-χ^2 fitting to this model for the outer rim of Ceres' disk shows that this model performs better than both Hapke's model and Minnaert model in this region (Fig. 3, green dots), although the residual is still greater than those of any models for the central part of the disk. The modeled parameters are listed in Table 3 at all three wavelengths. It is noticed that for the outer annulus, especially close to the edge of the disk, reflectance depends on both i and e with positive power law indices, meaning decreasing reflectance with both i and e.

5.4. Albedo maps

From photometric models derived above, we take the ratios of the observed brightnesses in the images to those predicted

Table 3
The modeled parameters of the modified Minnaert's model to the outer annulus of Ceres

λ (nm)	Range of i and e	Number of data points	A	k	j	RMS (%)
535	$50 < e \leqslant 75$	606	0.106	0.39	0.18	3.1
335	$50 < i, e < 60$	150	0.058	0.48	−0.19	1.3
	$i, e > 60$	237	0.073	0.52	0.10	3.3
223	$40 < i, e \leqslant 60$	170	0.050	0.37	−0.049	1.8
	$i, e > 60$	237	0.059	0.42	0.16	3.7

from the mean photometric parameters (Table 2), and scale the results by the predicted mean normal reflectance, r_n, to find normal reflectance images. Then by mosaicking them, normal reflectance maps can be constructed. It has to be noted, though, that the reflectance maps obtained by this method actually depend on an implicit assumption, that there is no variation in phase function and roughness across the whole surface. It is very possible that the roughness does not vary over the surface. First because we did not see any systematic variations of Hapke's modeling in the residuals as a function of i or e. Second, the fully relaxed shape of Ceres (Thomas et al., 2005), and the uniform surface of Ceres in terms of albedo and color (see later text), indicate that topography on Ceres probably has small variations. There might be variations in phase function parameters, such as g, B_0, and h. However, the currently available resolution is insufficient to distinguish the variations of different photometric parameters for Ceres. We therefore have to assume a constant phase function to represent surface albedo variations.

For the dark surface of Ceres of 0.073 SSA as found above, multiple scattering is always less than 3% of the total scattering under any geometries. If one assumes 10% SSA variation for Ceres, which is reasonable as found later, then the variation in multiple scattering will be about 4% for a roughness parameter $\bar{\theta} = 40°$, which is only responsible for 1% of the total reflectance variation. In other words, for Ceres' surface, more than 99% reflectance variation is accounted for by the variation in single scattering, which is directly proportional to the SSA, w. Therefore, under the assumption of constant g, B_0, and h, the albedo ratio maps described above not only represent the deviations of local normal reflectance, but also represent local deviations of SSA from its global average. The assumption of constant multiple scattering results in correct SSA map at V-band within an uncertainty of less than 1%, and even less for the SSA maps at the other two wavelengths because of the lower SSA. Therefore, in our following analysis and presentation of results, we present the deviation maps in a unit of percentage deviation from the corresponding averages at those wavelengths. We will not distinguish between the deviation maps, normal reflectance maps, and SSA maps in our text, as they only differ by constant factors (global mean normal reflectances and SSA's). Readers can convert those maps to the forms they need by multiplying them by the corresponding constants (Table 2) for their needs. Because of the small albedo variations of Ceres as we see later, this method of representing the albedo maps emphasizes subtle variations.

The procedure to find the deviation maps is as follows. First, for each HST image, we generated a model image using the disk-averaged parameters at the corresponding wavelength and the geometry of that image. Then we calculated the ratio of the real image to the model to find an image of the deviation from global average. In the next step, the deviation image as a disk is projected onto a planetocentric longitude–latitude coordinate system that is defined by Thomas et al. (2005) but with its longitude increasing toward east. After the projection maps have been made for all images, at each wavelength, we combine them, for each pixel, by taking the median of all maps covering that pixel, to construct a final map in Ceres' longitude–latitude system. Median filtering could also effectively remove cosmic rays that appear in single images. The deviation maps at three wavelengths are shown in Fig. 5. All these maps contain only the low-latitude area on Ceres (lower than $\pm 50°$ for F555W and F330W, and $\pm 40°$ for F220W), because only these parts on the disk can be modeled with small residuals. Although areas at higher latitude can be described by Minnaert model or our modified Minnaert model, the model residuals for those areas are comparable to the albedo variations we found for the center part of Ceres' disk. Therefore it is hard to trust the mapping of high-latitude areas. These maps are close to model-independent in the sense that we do not see any dependence of the residual on incidence and emission angles, thus no dependence on relative locations in the imaged disk. The resolution in these maps is enhanced compared to the original images, because for a particular area we have coverage from multiple images that include that area.

A pseudo-color map from the three maps is also constructed with F555W, F330W, and F220W deviation maps representing red, green, and blue, respectively (Fig. 6). Thus a red area in the pseudo-color map represents an area with high albedo relative to the average as seen through F555W filter, but relatively dark at the other two bands; if an area is yellow, a combination of red and green, then that area is relatively dark in only F220W filter, but relatively bright at the two other wavelengths; a white area means an area that is relatively bright at all three wavelengths. This map includes not only low-latitude areas where Hapke's model works well, but also high-latitude areas where Minnaert model or the modified Minnaert model was used. Therefore keep in mind that for high-latitude areas, the uncertainties in the deviation maps will be relatively large, and could be even higher than albedo variation for some areas. This pseudo-color map has been enhanced in contrast and color, and blurred by a scale of 3.5° with median filter, which is the corresponding pixel scale of our HST images at the equator on the surface of Ceres.

Since the albedo variation over Ceres' surface is only a few percent, we have to consider if the features seen on the maps are real or possibly due to artifacts from data processing, or even just random noise. For this purpose, we performed three tests. First, we made sure that the noise level in the original images is low compared to the variation of features so that they are not confused with surface features. To do this, the noise levels from raw images are estimated by the statistics of the background sky in those images, to be about 0.02, 0.04, and 0.4% of the average pixel readings over Ceres' disk for F555W, F330W, and F220W images, respectively. This level is much smaller than the albedo variation of about 2% at both F555W and F330W maps, and is about 1/5 of the albedo variation at the F220W map. Furthermore, the calculated standard deviations measured from different images for each longitude–latitude grid point is usually 1/5 to 1/4 of the global albedo variation. As shown earlier, the uncertainties caused by our approximation of constant multiple scattering is less than 1%. The uncertainty of relative photometry for HST/ACS images is usually better than 1%. Therefore although the distribution of albedo at any wave-

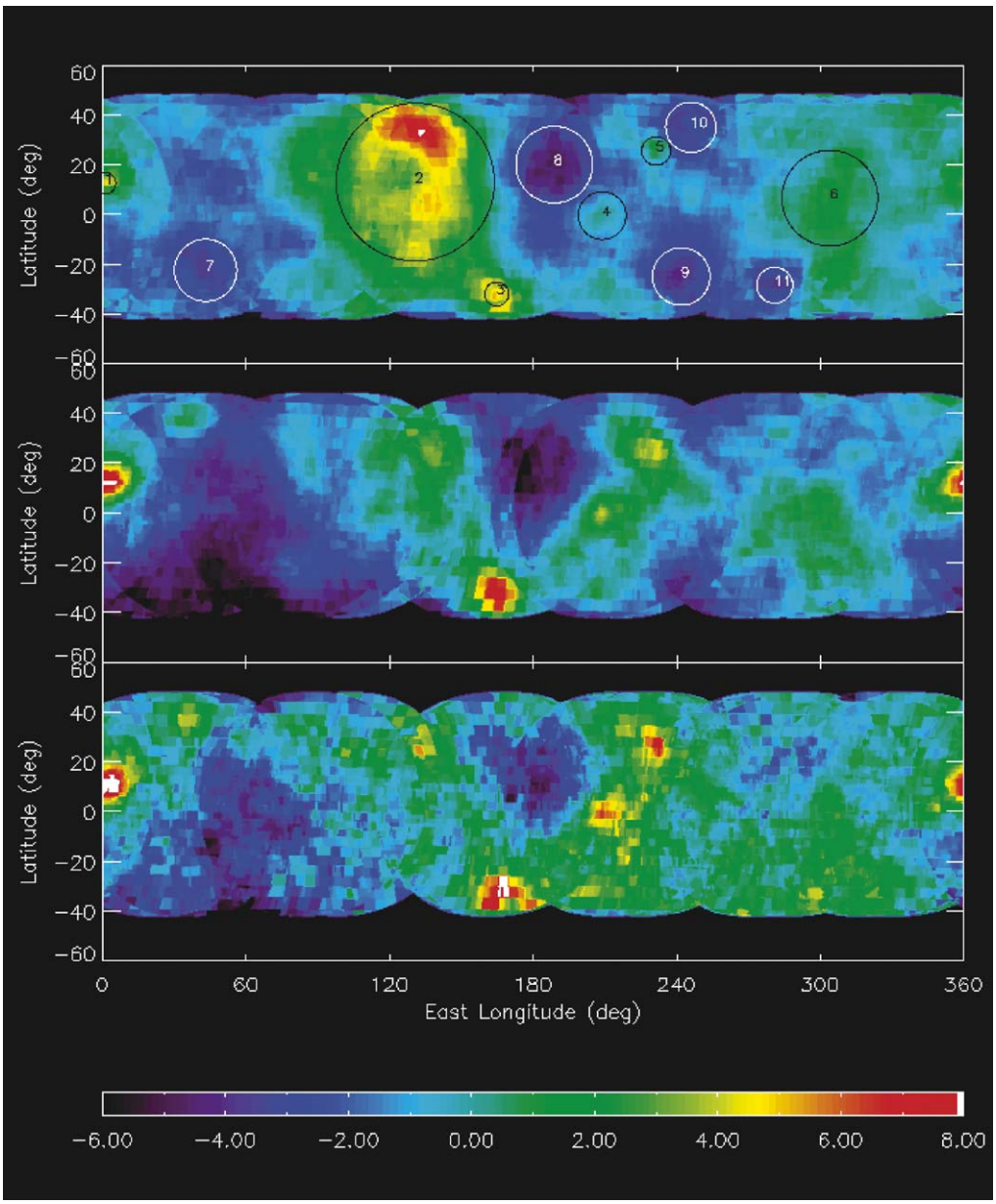

Fig. 5. The composite albedo deviation maps of Ceres through F555W (upper panel), F330W (middle panel), and F220W (lower panel) filters. The color bar represents the percentage deviation from their corresponding average values at three wavelengths (see Section 5.4 for more discussions). Readers can convert the deviation maps presented here to either SSA maps or normal reflectance maps by multiplying them by the corresponding averages over the disk (see Table 2 for modeled SSA or normal reflectance). Circles with numbers in the upper panel mark the features we identified. From #1 to #6 are bright features, and from #7 to #11 are dark features (see Section 5.5 and Table 4).

length is unimodal like a Gaussian, it does not necessarily mean that the features are totally random noise, especially the spatial distribution of albedo features do not appear to be random at all. The absolute photometric calibration error has the same effect for all pixels, thus does not affect the relative brightness of features. The photometric modeling is free of systematic deviations associated with incidence or emission angle, therefore is not likely to introduce artifacts.

Next, for each filter, we linked the images before being projected into longitude–latitude coordinates, while they are still disks, in the order of the time of observations, generating an animation showing the rotation of Ceres' disk. Then we linked the corresponding projected SSA maps in longitude–latitude plane into another animation, showing how the projection of the imaged hemisphere in each image moves in the fixed longitude–latitude coordinate when sub-Earth point moves around Ceres. Comparing these animations, we found that, while in the first animation, features like bright spots or dark spots move across the disk when Ceres rotates, the corresponding features in the second animation just sit still in their own longitude–latitude positions, with almost the same brightness level from frame to frame. This gives us confidence of two aspects: first, we see features in the raw HST images that are moving across the disk as Ceres rotates; and second, those features in all images are

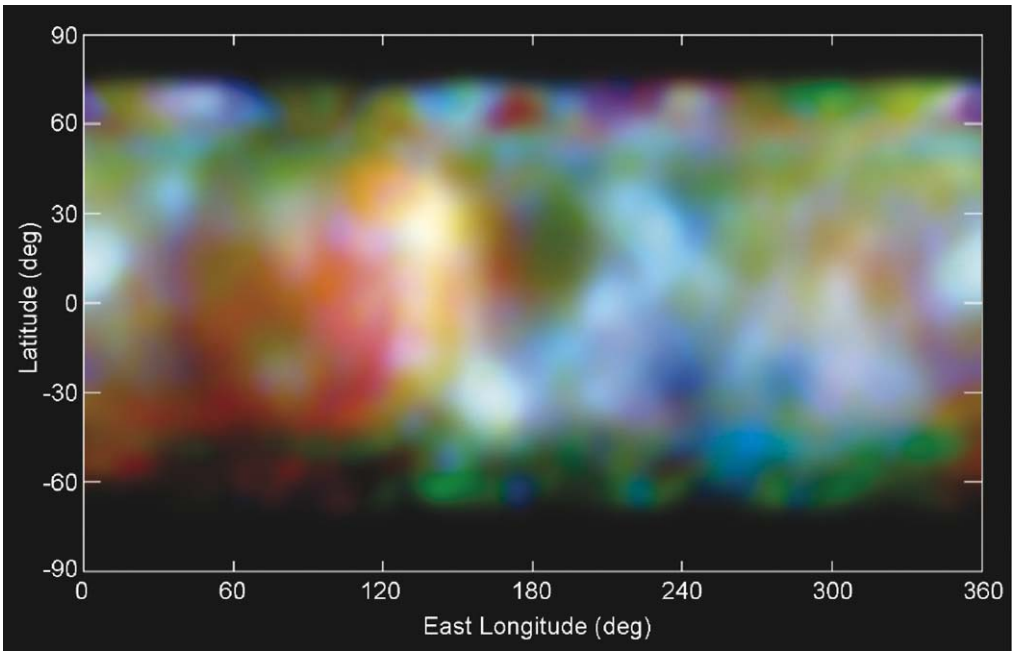

Fig. 6. The pseudo-color map of Ceres constructed from three albedo deviation maps shown in Fig. 5. F555W map is represented by red, F330W green, and F220W blue. See text (Section 5.4) for more discussions.

mapped into their correct locations on the longitude–latitude plane, and are positively enhanced to show themselves in the projections.

The third test is to use our SSA map and the shape of Ceres to produce synthetic disk-integrated lightcurves, and compare them with the observed lightcurves at three wavelengths. The synthetic lightcurves are plotted in Fig. 1 as dashed curves. We did not try to calibrate the absolute scale of the observed lightcurve and the synthetic lightcurve because the uncertainty in modeling the outer annulus is comparable with or higher than lightcurve amplitude, so that it is hard to calibrate the absolute brightness scale. Instead, the synthetic lightcurves were aligned with the observed ones in terms of average brightness levels. We notice that the synthetic lightcurves almost simulate the observed ones, indicating that the overall distribution of bright and dark terrains are retrieved correctly. The biggest difference appears at longitude about 0° at all three wavelengths, where the observed brightness is higher than the model predicted by 0.015 mag compared to the 0.04 mag total lightcurve amplitude. The underestimate of modeled lightcurve amplitude could be due to features at high latitude that cannot be modeled well. The slightly smaller lightcurve amplitude of synthetic lightcurves indicates that, at least to the scale comparable to the size of disk, we do not create artifacts. On the other hand, we may lose some features and fail to simulate their effect in the synthetic lightcurves.

To estimate the relative error of the deviation maps quantitatively, we calculated the standard deviation for each longitude–latitude location according to the total number of images for that location weighed by its cosine of emission angle in each image. This takes into account the change in pixel scale due to the projection from disks to the longitude–latitude plane. We found that for the area with latitude less than 50°, the error does not exceed 3% in the F555W map, and peaked at 1% level. For the F330W map, the same analysis shows a maximum error of 4% for low-latitude areas, with most at 1.3%. The map of the F220W filter shows some large errors greater than 10% and up to 50% for less than 3% of the total area of the low-latitude surface, but most of it is at the 2% level. All those tests and the error estimate convince us that, for areas with latitude lower than 50°, at least big features seen on the maps are real. Small features could also be real, but their shapes may have been circularized due to our limited spatial resolution.

5.5. Albedo features

The albedo features show local heterogeneity on Ceres, although variations from the average are very small. The features are quite consistent but with different relative strengths at three wavelengths (Fig. 5, Table 4). The most obvious, #2, the big bright area, is centered at 130° longitude and 15° latitude, about 60° across, with an elongated shape. Other small features appear to be circular, including the one at 0° longitude (#1, defining the longitude system), and the series of features (#3–5) along a diagonal line to the right of the biggest bright area. A dark area (#7) to the left of the biggest bright area is open toward the south pole. Another dark area (#8) close to the equator and to the right of #2 has a bright rim around it, and is consistently dark at all three wavelengths. Its latitude is consistent with the "Piazzi" feature reported previously (Parker et al., 2002), but a certain identification cannot be made due to insufficient longitude constraints of the earlier observations.

Comparing the albedo maps at three wavelengths, or looking at the pseudo-color map, we see that bright features can be divided into at least two different spectral groups. One group includes #2, which is relatively redder by 8% than the sec-

Table 4
Summary of features on Ceres' surface. Their albedo at 535 nm for #1 to #6 are brighter than surrounding background, and for #7–11 darker than surrounding area

Index	Longitude (°)	Latitude (°)	Size (°)	V-band SSA (×0.073)	335–535 nm color (mag)
1	1	12	4	1.04	0.40
2	130	13	33	1.04	0.47
3	164	−32	5	1.04	0.41
4	208	−1	10	1.00	0.42
5	231	25	6	1.01	0.41
6	303	−23	13	1.02	0.46
7	43	−23	13	0.96	0.47
8	188	20	16	0.96	0.44
9	241	−25	12	0.96	0.44
10	245	35	10	0.97	0.43
11	280	−29	7	0.96	0.43

ond group, including #1 and #3–5. This color difference is confirmed by the different shapes of lightcurves at three wavelengths (Fig. 1), and by the different trends of their spectra as shown later. The spectral variation between these two groups of features, and their different shapes, may indicate different compositions and origins.

6. Discussion

6.1. Roughness parameter

Hapke's theory for rough surface was derived assuming low albedo (weak multiple scattering) and low roughness ($\tan(\theta)$ not too high) (Hapke, 1993). The roughness parameter of Ceres is modeled to be as high as 44°. Whether or not it has a physical meaning deserves discussion. The modeled parameters provide good descriptions of the limb darkening properties of Ceres' disk, at least for the central part. Since we did not see any systematic deviations with respect to incidence angle and emission angle, with the small residual of the model, it is fair to say that the geometric effects on the reflectance associated with μ_0 and μ have been removed, and the average albedo of the surface has been measured accurately. In this sense, the deviation maps of reflectance as derived above are valid. The modeled roughness parameter, $\bar{\theta}$, may or may not be the real roughness of the surface.

However, earlier results by other observational means also suggested high surface roughness of Ceres. Mitchell et al. (1996) reported 20°–50° RMS slope at scales larger than centimeters by analyzing radar echoes from Ceres. In addition, both the radar observations (Mitchell et al., 1996) and thermal modeling (Saint-Pé et al., 1993) suggest the possible existence of a complex roughness structure such as fractal topography. Thus the high roughness of Ceres could be real, but probably in a form that is different from the underlying assumptions in Hapke's model, where the distribution of the normal directions of surface facets on a rough surface was treated as isotropic with a Gaussian distribution (Hapke, 1993). This could also be a possible reason that Hapke's model fails at high i and e for Ceres—simply because the anisotropic distribution of high slopes has a large effect when the average surface normal differs too much from incident light and the line of sight. When either or both i and e are high, the high roughness tends to violate the inherent assumption that was made to derive Hapke's model for rough surfaces. The smoothness of Ceres' limb suggests that its highest relief does not exceed 5 km (Thomas et al., 2005), while radar observations also showed a smooth surface at scales of centimeters to decimeters (Mitchell et al., 1996). Thus if the high photometric roughness is real, it must be at scales between meters and kilometers, and widespread all over the surface. The surface of Ceres is probably made of very smooth materials at small scales, either particles with mirror-like surfaces, or coating of fine particles, but saturated with small craters, or a blocky, chaotic surface at the sizes of tens of meters to kilometers. Unfortunately, the size scale of roughness cannot be directly observed by photometric methods from our current HST images. Dawn will provide images at resolutions as high as 10 m/pixel (Russell et al., 2004), showing surface topography in more detail.

A related question is, whether or not the modeled single scattering albedo, w, is real, provided that a high surface roughness is derived from the same modeling. From a data modeling point of view, the covariance factor of the two modeled parameters, w and $\bar{\theta}$, from our data is about 0.15, meaning that the modeling to those two parameters are almost orthogonal. Therefore the interpretation of roughness, $\bar{\theta}$, almost does not affect the interpretation of w. And again, compared with earlier observations (Millis et al., 1987; Lagerkvist and Magnusson, 1990), as well as our direct measurements from images, the modeled geometric albedo from the fitted parameters is consistent with all of them. Thus the modeled single scattering albedo should be real.

6.2. Color variations

The distributions of the SSA of Ceres at three wavelengths all show a unimodal shape with very narrow ranges (Fig. 7). From the albedo maps, we can derive the color variations of Ceres' surface by dividing any two of them. Such ratio maps are shown in Fig. 8. The corresponding histograms are shown in Fig. 9. It has to be kept in mind, though, that, because the uncertainty in the deviation maps is about 2%, the error in the color ratio maps will be about 3%. Given the color variations of Ceres of only about 3% standard deviation, comparable with the uncertainty, we have to be cautious in interpreting the color features we see on these color ratio maps. Only big features with very distinctive color ratios, and consistent with the difference of lightcurves at different wavelengths should be considered to possibly be real. For example, in the color ratio map of F330W/F555W, we believe that the big red region at about 100° longitude and the big blue region at about 220° longitude are spectrally different. But the variations within the above two features may not be real.

As stated in the previous section, the eleven features can be grouped into two different spectral types as shown in Fig. 10, where the albedo deviations of each feature is plotted as a function of wavelength. Thus what are shown here are not the spectra of the features, but their deviation from the globally av-

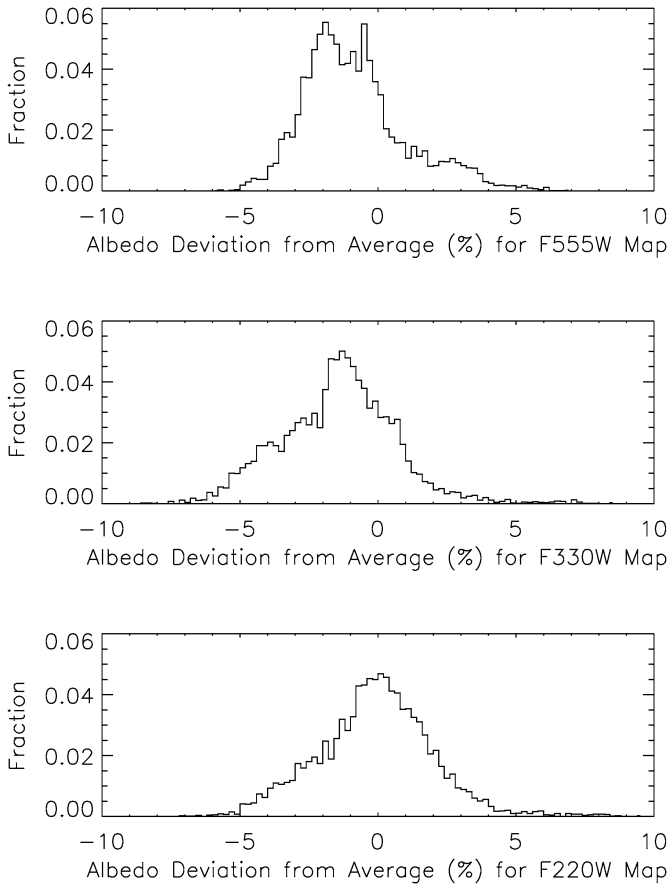

Fig. 7. The histograms of the albedo deviations from their corresponding averages at three wavelengths. The averages of albedo deviations are not exactly zero due to the uncertainties introduced in mapping and mosaicking. But they are all within the estimated uncertainties for all three maps.

eraged spectrum. Two spectrally distinct groups can be clearly shown here: One includes features #2, #6, and #7, with their spectra almost aligned with the average spectrum of Ceres, but slightly redder (2%); another group includes all other features, with their spectra slightly bluer than average by up to 6%. Caution has to be used when interpreting the spectral difference between features. The uncertainties within the albedo deviation maps is about 2–3% as shown in the upper right corner of Fig. 10, so the subtle difference between the spectra of features is possibly not real. Since we have not found good interpretations for the UV spectral absorption band in Ceres' spectrum, interpretations for the subtle variation of the spectra of these features are not possible. The color and albedo variations between features may indicate different compositions and/or origins. They may also represent terrain deformed by expansion and/or contraction as suggested by McCord and Sotin (2005).

6.3. The uniform surface of Ceres

Fig. 11 shows the range of normal reflectances for some Solar System small bodies, in the order of their heliocentric distance. The axis of normal reflectance is a logarithm scale, so that the variations as expressed by magnitudes are directly proportional to the lengths of lines. At the resolution of our HST observations (60 km), the reflectance variation of Ceres is much smaller than all asteroids and many icy satellites shown here, but close to some icy moons of the giant planets such as Miranda, and Umbriel. Below our resolution, there could be albedo patterns with large variations but on the scales of a few kilometers. Given the size of Ceres about 1000 km across, and imaged to more than 750 pixels in our observations, it is not likely that such patterns are spread over the surface to affect the global albedo distribution significantly, resulting in a different albedo distribution if imaged at a higher resolution. The range of albedo could be possibly extended by a small fraction, though. Therefore, Ceres' surface is probably one of the most uniform surfaces of small Solar System bodies measured to date. Its clear differences from other known main-belt rocky asteroids, its unique spectrum, and a possibly high water fraction, indicate that Ceres has clearly taken a different evolutionary path than other rocky asteroids. Its distance from the Sun may have set its evolution between that of rocky bodies and icy bodies. Its high water fraction may suggest the importance of water in its evolution as for icy bodies (McCord and Sotin, 2005).

Although there is a lack of spectral evidence for water ice on Ceres' surface (Larson et al., 1979), the presence of a UV emission at 308 nm to the north of Ceres' limb suggests the existence of a low abundance of OH molecules that can only be produced by photodissociation of water in sunlight. The corresponding H_2O production rate of 10^5–10^6 times smaller than that of an active comet may be evidence for the existence of water ice on or beneath the surface (A'Hearn and Feldman, 1992). The strong absorption feature at about 3 μm (Lebofsky et al., 1981) was interpreted as being caused by water molecules or structural OH groups embedded in between layers of clay minerals (Lebofsky et al., 1981; Feierberg et al., 1981), and is also attributed to an ammoniated clay mineral (King et al., 1992). The best density calculations of Ceres imply about 25% water (Thomas et al., 2005; McCord and Sotin, 2005). Thus the most acceptable composition of the surface layer of Ceres is thought to consist of metamorphosed and/or aqueously altered clay minerals, and a large amount of water inside. Starting from these results, the most recent evolutionary model (McCord and Sotin, 2005) predicts that water has played an important role in heat transport and redistribution inside Ceres in its early evolutionary history.

Here we would like to offer a very general picture of the evolution of Ceres. Heated by the energy from gravitational accretion and probably radioactive decay such as ^{26}Al (Grimm and McSween, 1989) shortly after its formation, Ceres probably differentiated, with water ice reaching its surface (McCord and Sotin, 2005), formed an icy crust globally, and may have had ice tectonics or water volcanism, like what is happening today on, e.g., Europa. Such geological activity would resurface Ceres by mixing and/or depositing minerals on the surface, erasing major albedo and morphological features, if any. The lack of a dynamical family of small asteroids associated with Ceres, unlike Vesta's vestoids, is consistent with an icy crust that would not produce such a family. The surface of Ceres was hydrated and/or

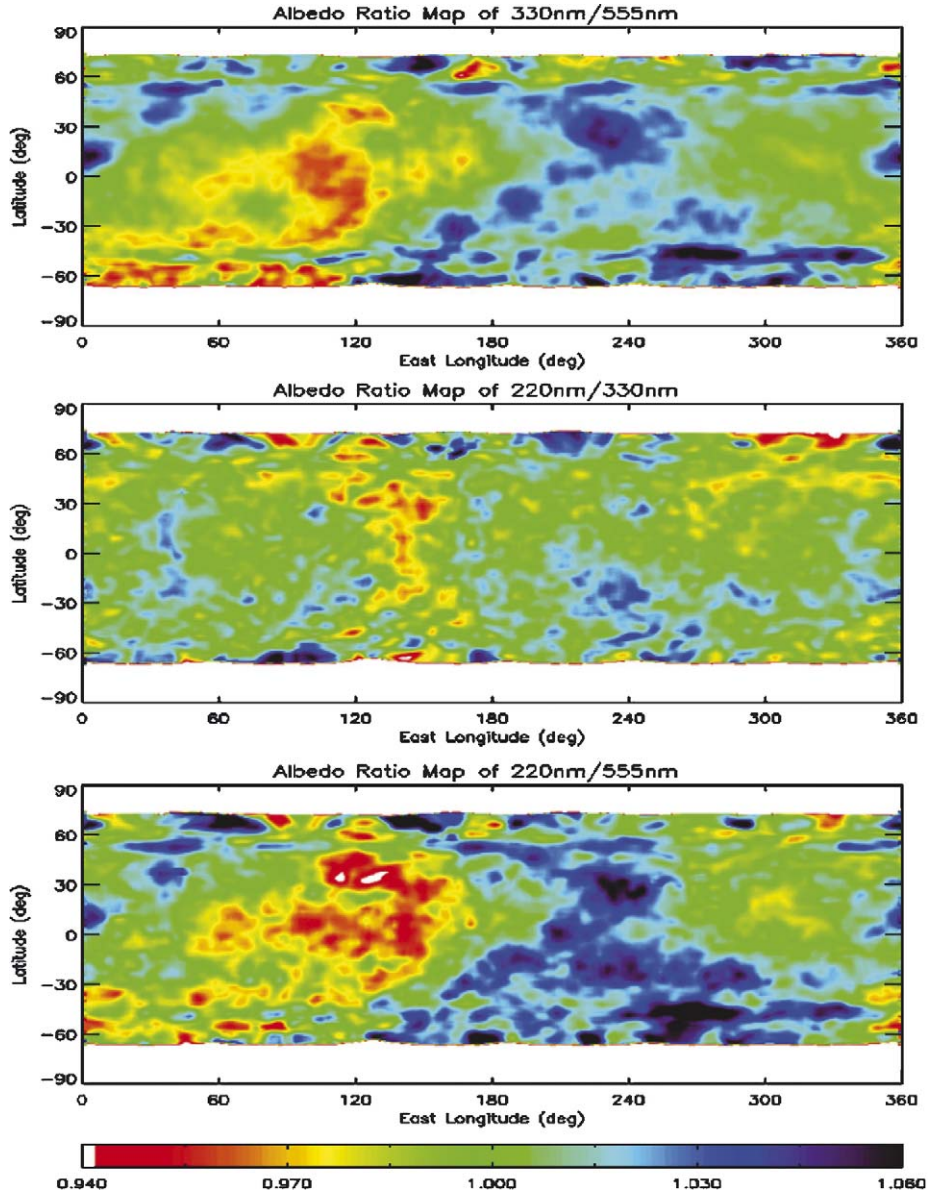

Fig. 8. The color ratio maps of Ceres, derived by dividing the albedo deviation maps at two different wavelengths. Note, however, because the relative uncertainties between features in the color ratio maps are comparable with the standard deviations of the color ratio (Fig. 9), caution has to be used when considering whether color features in these maps are real or not.

ammoniated during this time. However, unlike Europa, which has continuous energy input from Jupiter's tidal perturbation to sustain activity today, Ceres has cooled down as its internal energy sources depleted quickly, and all activities tapered off as its temperature decreased. This does not necessarily imply that water ice exists on its surface today. Comets 19P/Borrelly and 9P/Tempel 1, containing a large fraction of interior water ice, has a dry and hot surface (Soderblom et al., 2004; A'Hearn et al., 2005). Actually water ice should not be expected on the surface of Ceres, because it is always within 3 AU (perihelion 2.55 AU, aphelion 2.99 AU), a canonical distance within which water is not stable on the surface of any small body (Cowan and A'Hearn, 1979). The actual temperature of the warmest area on Ceres was measured to be 235 ± 4 K (Saint-Pé et al., 1993), not favoring the existence of amorphous water ice or crust. Water ice on Ceres' surface, if it existed, must have been sublimated over time and escaped from its weak gravity, leaving behind hydrated and ammoniated silicates. If there is still some water ice on its surface today, it must be on the poles where the least sunlight is received. Unlike comets, which outgas periodically at perihelion and alter their surfaces, Ceres' surface is geologically dead today, with a hydrated but uniform surface left behind.

In 2014, the Dawn mission is scheduled to observe Ceres' surface morphology, determine the crater density, and thereby infer the age of the surface. Dawn can measure the mineral composition with visible-IR spectroscopy, and the water-related hydrogen fraction both on the surface and underneath with gamma-ray/neutron spectroscopy. This will help us very much in understanding the history of Ceres.

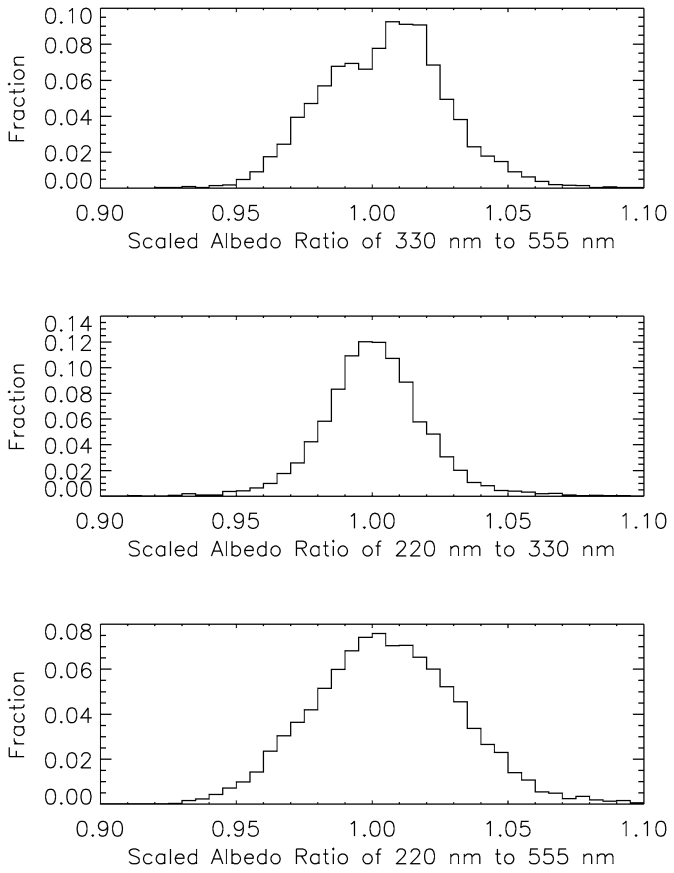

Fig. 9. The histograms of the color ratio maps. Three panels correspond to the three color ratio maps shown in Fig. 8.

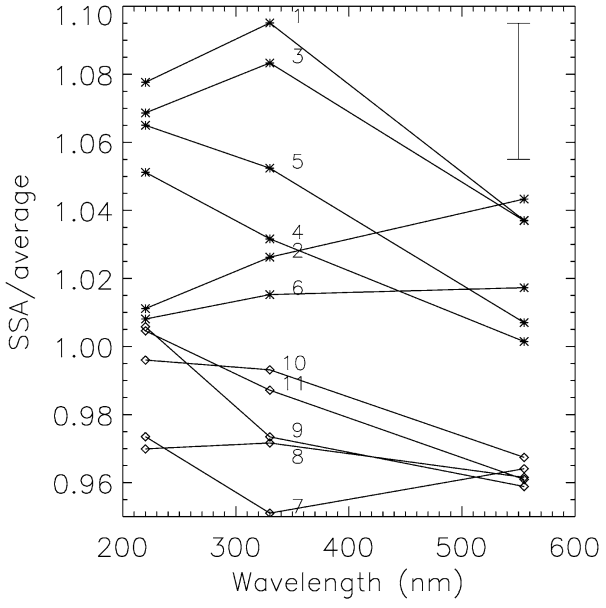

Fig. 10. The plot of spectral deviation from the average spectrum of Ceres for the eleven features as identified in Table 4. These spectra are plotted as the percentage deviation from the average spectrum of Ceres (Fig. 2). What is emphasized here is the subtle deviations of the spectra of features from the average. However, note that the typical error bar of absolute photometric calibration as shown in the plot are about 2%, which is comparable with the spectral difference between some features.

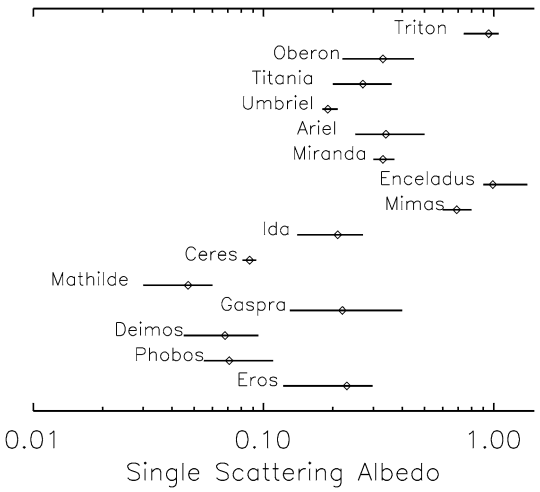

Fig. 11. Lines represent the range of normal reflectance for some asteroids and satellites, with diamonds the corresponding averages. Objects are ordered by heliocentric distance from bottom to top for the purpose of clarity. Data are all V-band unless otherwise specified below. Eros's range of normal reflectance is scaled proportionally from its reflectance at $i = 30°$ and $e = 0°$ as found in the literature. References are: Eros: Li et al. (2004); Murchie et al. (2002); Phobos: Simonelli et al. (1998); Deimos: Thomas et al. (1996); Gaspra (410 nm): Helfenstein et al. (1994); Mathilde: Clark et al. (1999); Ceres: this work; Ida: Helfenstein et al. (1996). The measurement for the following six objects are at 480 nm: Mimas: Verbiscer and Veverka (1992); Enceladus: Verbiscer and Veverka (1994); Miranda, Ariel, Umbriel, Titania: Buratti and Mosher (1991) Oberon: Helfenstein et al. (1991); Triton: Hillier et al. (1994).

7. Conclusions

In conclusion, Ceres is observed with HST ACS/HRC through three broadband filters centered at 535, 335, and 223 nm. Images were taken at phase angles from 5.4° to 7.5°, covering more than one full rotation of Ceres. The pixel scale of HST observations is 30 km/pixel, with the disk of Ceres imaged into more than 750 sunlit pixels, enabling disk-resolved photometric analysis. The lightcurves of Ceres from the HST observations are found to be consistent with earlier observations (Tedesco et al., 1983). Lightcurve variations at the three bandpasses indicate color variations across the surface. The geometric albedo of Ceres at the above three wavelengths are measured to be 0.087 ± 0.003, 0.056 ± 0.002, and 0.039 ± 0.003, respectively. Applying a correction factor of 0.04 mag, we derived the V-band geometric albedo of Ceres to be 0.090 ± 0.003, consistent with earlier measurements (Tedesco, 1989). A spectrum of Ceres is constructed from our HST observations and earlier ones (Chapman and Gaffey, 1979; Parker et al., 2002), showing a strong absorption band centered at about 280 nm with 30% reflectance of that at V-band. This spectral feature is not due to terrestrial atmospheric ozone contamination, but its source has not been identified. Combined with the shape model of Ceres from Thomas et al. (2005), disk-resolved Hapke's modeling yields a good fit to the central portion of Ceres' imaged disk. Minnaert model and a model that is modified from the Minnaert model yield a better fit to the reflectance at the outer annulus of Ceres' disk. The single scattering albedo of Ceres at the above three wavelengths are modeled to be 0.073 ± 0.002, 0.046 ± 0.002, and 0.032 ± 0.003,

respectively. The surface of Ceres is found to be very rough at the scales between ten kilometers to meters, with a photometric roughness parameter $44° \pm 5°$. The deviation maps of albedo from the averages at three wavelengths are produced for Ceres, showing small variations at spatial scales >60 km compared to other asteroids and some icy satellites. Eleven surface features defined by albedo and spectrum are identified. The uniformity of albedo, together with the large water content as indicated by its mean density (Thomas et al., 2005), suggest that Ceres could have been resurfaced, probably by melted water or ice, after the heavy bombardment phase of Solar System formation, although small craters or other topographic features below the resolution (<60 km) of these data may exist. In short, Ceres is proving to be a very important and unique Solar System object, a key to understanding the early Solar System processes that occurred in the proto-terrestrial planets.

Acknowledgments

Support for HST GO Program #09748 was provided by NASA through a grant from the Space Telescope Science Institute, which is operated by the Association of Universities for Research in Astronomy, Inc., under NASA Contract NAS 5-26555. The authors would like to thank T.B. McCord, P. Helfenstein, and B. Hapke for helpful discussions of this work. Thank N.J. Goldman on helping prepare tables and figures. Thank you to A.J. Verbiscer and J.K. Hillier for their reviews that have helped improve this manuscript.

Appendix A

A.1. Photometric calibration

The photometric calibration for our HST images was done in two steps. First, all images were calibrated to reduced magnitude at $r = 1$ AU and $\Delta = 1$ AU. The procedure has been standardized and summarized in relevant HST documentation (Pavlovsky et al., 2005). Three keywords in the image headers were used to carry out this step: the exposure time, EXPTIME, and two photometry keywords, PHOTFLAM, the inverse sensitivity in ergs cm^{-2} Å^{-1} DN^{-1}, and PHOTZPT in magnitude, the HST magnitude zero point. Their values for the three filters are listed in Table 5. The formula we used was

$$M = -2.5\log\left(\frac{\mathrm{DN}}{\mathrm{EXPTIME}} \times \mathrm{PHOTFLAM}\right) + \mathrm{PHOTZPT} - 5\log r - 5\log\Delta, \tag{A.1}$$

where DN is pixel value, r and Δ are the heliocentric distance and Earth range, respectively, measured in AU.

The second step is to convert reduced magnitude to reflectance unit I/F, with the formula derived to be

$$I/F = \frac{1}{A}10^{(M_0 - M)/2.5}, \tag{A.2}$$

where A is the pixel scale in km^2 pixel^{-1}, and M_0 is a constant resulting from the apparent magnitude of the Sun, $m_\odot$, through the corresponding bandpass,

$$M_0 = m_\odot + 2.5\log\pi + 5\log(1\ \mathrm{AU}/1\ \mathrm{km}) = 42.12 + m_\odot. \tag{A.3}$$

The apparent magnitude of the Sun through F555W filter was obtained by applying the 0.04 mag correction (Pavlovsky et al., 2004, Table 10.2) to the V-band magnitude of the Sun, −26.75 (Cox, 1999). M_0 is calculated to be 15.41 mag for F555W filter. Combining Eqs. (A.1), (A.2), and (A.3), the formula we used to convert DN number of HST images to I/F reads

$$I/F = r_0 \times \frac{\mathrm{DN}}{\mathrm{EXPTIME}} \times \frac{r^2\Delta^2}{A}, \tag{A.4}$$

where

$$r_0 = 10^{(42.12 + m_\odot - \mathrm{PHOTZPT})/2.5} \times \mathrm{PHOTFLAM} \tag{A.5}$$

is a constant for each filter, meaning the required reflectance for a 1-km^2 area at 1 AU from both the Sun and HST in order to produce one DN per one second exposure time as imaged by ACS/HRC through the corresponding filter. r_0 for the F555W filter was calculated to be 1.21×10^{-4} (Table 5).

Table 5
Calibration constants for Ceres HST images

Filter	PHOTFLAM (ergs cm^{-2} Å^{-1} DN^{-1})	PHOTZPT (mag)	$m_\odot$ (mag)	r_0[a]
F555W	3.020×10^{-19}	−21.1	−26.71	1.21×10^{-4}
F330W	2.237×10^{-18}	−21.1	−25.85	1.97×10^{-3}
F220W	8.113×10^{-18}	−21.1	−22.60	0.144

[a] As defined in Eq. (A.5): $r_0 = 10^{(42.12 + m_\odot - \mathrm{PHOTZPT})/2.5} \times \mathrm{PHOTFLAM}$.

In order to calculate r_0 through F330W and F220W filters, the apparent magnitudes of the Sun as seen through these two filters have to be calculated. This is done by taking a high resolution spectrum of the Sun (A'Hearn et al., 1983; Lean et al., 1992), and modulating it by the throughput of the whole ACS/HRC imaging system including optics, filters, and CCD response, as found from relevant HST documentations (Pavlovsky et al., 2004), and then calculating the average flux per unit wavelength:

$$F_i = \frac{\int F(\lambda)T_i(\lambda)\,\mathrm{d}\lambda}{\int T_i(\lambda)\,\mathrm{d}\lambda}, \tag{A.6}$$

where F_i is the average solar flux per unit wavelength through filter i, $T_i(\lambda)$ is the total throughput of the imaging system, $T_i(\lambda) = T_o \times T_{fi} \times T_{\mathrm{CCD}}$, including the throughput of optics (T_o), filter i (T_{fi}), and CCD response (T_{CCD}). After the average solar fluxes per unit wavelength through F330W filter and F220W filter relative to that through F555W filter are calculated, the magnitudes of the Sun through those two filters can be calculated. However, it has to be noted that there exists about 10% red leak for ACS/HRC F220W filter when imaging stars with solar type spectra (Pavlovsky et al., 2004, Table 4.7). Thus in the calculation of the inband magnitude of the Sun through the F220W filter, we put a spectral cutoff at 320 nm to avoid including out-of-band flux. The calculated apparent magnitudes of the Sun and corresponding r_0's are summarized

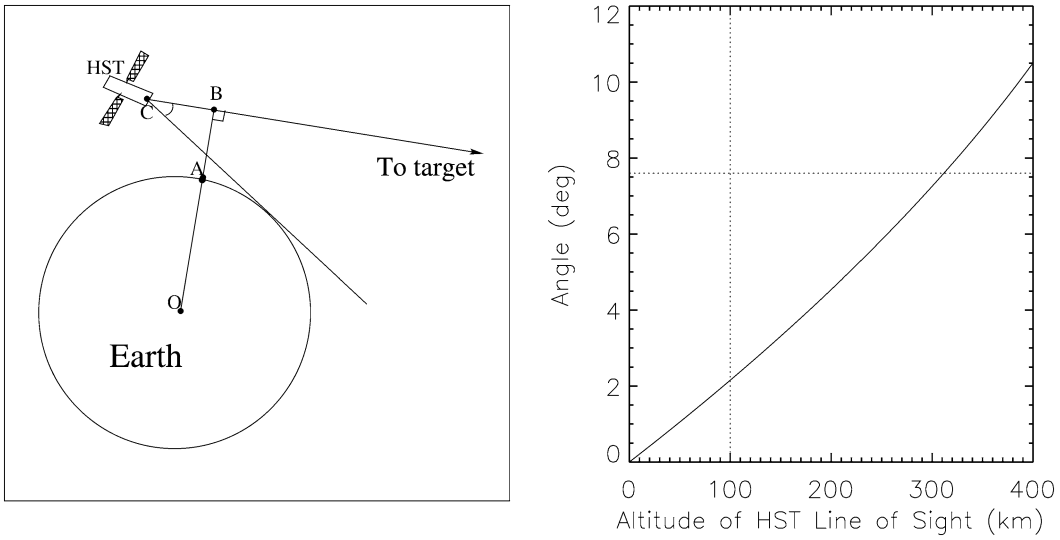

Fig. 12. The angular distance from Earth limb to a particular target as seen from HST (angle ACB), is plotted as a function of the altitude (line AB) of HST line of sight (line CB) from Earth's surface. Left panel shows a diagram of the geometry, and right panel shows the plot. The minimum allowed angular separation of the line of sight of HST from Earth limb, 7.6° (horizontal dotted line), determines that the lowest altitude of the light of sight of HST is always higher than about 310 km, much higher than the altitude of terrestrial atmospheric ozone, which is about 100 km (vertical dotted line).

in Table 5. The absolute photometric calibration of ACS/HRC images should be generally better than 2% (Pavlovsky et al., 2004). Considering the uncertainties of the high resolution solar spectra we used, and the throughput characteristics of ACS imaging system, we take 3% as the uncertainty of the absolute photometric calibration for images through filters F330W. The uncertainty of absolute photometry through filter F220W will be estimated next in the analysis of the significant red leak for this filter.

The resultant I/F of Ceres through the F220W filter obtained using the above calibration procedure contains a considerable amount of red leak, which can be estimated with the following analysis. Let the throughput function of F220W filter to be $T(\lambda) = T_0(\lambda) + T_1(\lambda)$, where $T_0(\lambda)$ is the inband throughput, and $T_1(\lambda)$ is the out-of-band throughput. For a solar spectrum, the total flux received by the detector through this filter can be written as the sum of inband flux, F_0, and out-of-band flux F_1, where

$$F_j = \int F_\odot(\lambda) T_j(\lambda)\,\mathrm{d}\lambda, \quad j = 0 \text{ or } 1. \tag{A.7}$$

$F_\odot(\lambda)$ is the solar flux spectrum prior to entering the filter. Table 4.7 in Pavlovsky et al. (2004) shows that $F_0 = 90.2\% \times (F_0 + F_1)$. The total flux of Ceres received through the F220W filter also contains two components, an inband flux, F'_0, and an out-of-band flux, F'_1, expressed as,

$$F'_j = \int r(\lambda) F'_\odot(\lambda) T_j(\lambda)\,\mathrm{d}\lambda, \quad j = 0 \text{ or } 1, \tag{A.8}$$

where $r(\lambda)$ is the reflectance of Ceres as a function of wavelength, and $F'_\odot$ is the solar flux spectrum, different from $F_\odot$ in Eq. (A.7) by a constant scaling factor, C. If we write the average reflectance of Ceres within the bandpass of F220W filter as

$$r_{\mathrm{F220W}} = \frac{\int r(\lambda) F'_\odot(\lambda) T_0(\lambda)\,\mathrm{d}\lambda}{\int F'_\odot(\lambda) T_0(\lambda)\,\mathrm{d}\lambda}, \tag{A.9}$$

then the F'_0 for Ceres is, $F'_0 = r_{\mathrm{F220W}} \times C \times F_0$, where F_0 is defined in Eq. (A.7). In addition, because the spectrum of Ceres is flat within ±10% at wavelengths longer than 400 nm, we can write the F'_1 term for Ceres as $F'_1 = r_1 \times C \times F_1$, where F_1 is defined in Eq. (A.7), and r_1 is the average reflectance of Ceres at out-of-band wavelength for F220W filter. If we assume that r'_{F220W} is the average reflectance of Ceres calculated from the total flux through F220W filter, including both inband flux and out-of-band flux,

$$r'_{\mathrm{F220W}} = \frac{\int r(\lambda) F'_\odot(\lambda)[T_0(\lambda) + T_1(\lambda)]\,\mathrm{d}\lambda}{\int F'_\odot(\lambda) T_0(\lambda)\,\mathrm{d}\lambda}, \tag{A.10}$$

then the total flux of Ceres through F220W filter is $r'_{\mathrm{F220W}} F_0 \times C$. We have

$$r'_{\mathrm{F220W}} F_0 = r_{\mathrm{F220W}} F_0 + r_1 F_1. \tag{A.11}$$

Simple manipulation shows that

$$\frac{r_{\mathrm{F220W}}}{r'_{\mathrm{F220W}}} = 1 - 0.109 \times \frac{r_1}{r'_{\mathrm{F220W}}}. \tag{A.12}$$

If we take $r_1 = r_V$, the reflectance at V-band, and measure r_V from F555W filter, and measure r'_{F220W} from F220W filter, we found that the real reflectance of Ceres through F220W filter is 80.2% of the directly converted value from Eq. (A.4) and the calibration constants in Table 5 without considering the red leak. The uncertainty in the absolute photometric calibration for images through F220W filter was estimated to be about 8%, as combining all sources of error in the estimate of red leak, including uncertainties of r'_{F220W} and r_V, and up to 10% fluctuation of the spectrum of Ceres at visible wavelengths longer than 400 nm.

A.2. Ozone contamination

If the line of sight of HST is too close the Earth, then it could possibly pass through the top of terrestrial atmosphere.

The images observed at UV (specifically at 290 nm vicinity) could pick up the Hartley band of terrestrial atmospheric ozone (O_3). In order to determine whether or not our images are contaminated by terrestrial atmosphere, we calculated the angular distance from Earth's limb to a particular target as seen from HST, as a function of the altitude of the telescope's line of sight (line AB in Fig. 12). The orbital altitude of HST is taken to be the minimum, 580 km in our calculation. To shield HST from scattered light from Earth's limb and terrestrial atmosphere, it is not allowed to point within 7.6° of the dark limb of the Earth, or 15.5° of any illuminated portion of the Earth (Hubble Space Telescope Primer for Cycle 12). Therefore, as seen from the horizontal dotted line in Fig. 12, the line of sight of HST is never closer than about 310 km from Earth's limb. This is much higher than the bulk altitude of terrestrial atmospheric ozone, which is <100 km from Earth's surface, as shown by the vertical dotted line in Fig. 12. Therefore, all HST observations should be free of ozone contamination from the terrestrial atmosphere.

References

A'Hearn, M.F., Feldman, P.D., 1992. Water vaporization on Ceres. Icarus 98, 54–60.

A'Hearn, M.F., Ohlmacher, J.T., Schleicher, D.G., 1983. A high resolution solar atlas for fluorescence calculations. Tech. Report. Astronomy Program of Univ. of Maryland, College Park, AP 83-044.

A'Hearn, M.F., and 32 colleagues, 2005. Deep Impact: Excavating Comet Tempel 1. Science 310, 258–264.

Ahmad, I.I., 1954. Photometric studies of asteroids. IV. The light-curves of Ceres, Hebe, Flora, and Kalliope. Astrophys. J. 120, 551–559.

Bell, J.F., Davis, D.R., Hartmann, W.K., Gaffey, M.J., 1989. Asteroids—The big picture. In: Binzel, R.P., Gehrels, T., Matthews, M.S. (Eds.), Asteroids II. Univ. of Arizona Press, Tucson, pp. 921–945.

Bowell, E., Hapke, B., Domingue, D., Lumme, K., Peltoniemi, J., Harris, A.W., 1989. Application of photometric models to asteroids. In: Binzel, R.P., Gehrels, T., Matthews, M.S. (Eds.), Asteroids II. Univ. of Arizona Press, Tucson, pp. 524–556.

Buratti, B.J., Mosher, J.A., 1991. Comparative global albedo and color maps of the uranian satellites. Icarus 90, 1–13.

Chapman, C.R., Gaffey, M.J., 1979. Spectral reflectances of the asteroids. In: Gehrels, T. (Ed.), Asteroids. Univ. of Arizona Press, Tucson, pp. 1064–1089.

Chapman, C.R., Salisbury, J.W., 1973. Comparisons of meteorite and asteroid spectral reflectivities. Icarus 19, 507–522.

Clark, B.E., Veverka, J., Helfenstein, P., Thomas, P.C., Bell, J.F. III, Harch, A., Robinson, M.S., Murchie, S.L., McFadden, L.A., Chapman, C.R., 1999. NEAR photometry of Asteroid 253 Mathilde. Icarus 140, 53–65.

Cowan, J.J., A'Hearn, M.F., 1979. Vaporization of comet nuclei—Light curves and life times. Moon Planets 21, 155–171.

Cox, A.N., 1999. In: Cox, A.N. (Ed.), Allen's Astrophysical Quantities, fourth ed. Athlone Press, London.

Drummond, J.D., Fugate, R.Q., Christou, J.C., Hege, E.K., 1998. Full adaptive optics images of asteroids Ceres and Vesta: Rotational poles and triaxial ellipsoid dimensions. Icarus 132, 80–99.

Feierberg, M.A., Lebofsky, L.A., Larson, H.P., 1981. Spectroscopic evidence for aqueous alteration products on the surfaces of low-albedo asteroids. Geochim. Cosmochim. Acta 45, 971–981.

Gaffey, M.J., Bell, J.F., Cruikshank, D.P., 1989. Reflectance spectroscopy and asteroid surface mineralogy. In: Binzel, R.P., Gehrels, T., Matthews, M.S. (Eds.), Asteroid II. Univ. of Arizona Press, Tucson, pp. 98–127.

Gehrels, T., Owings, D., 1962. Photometric studies of asteroids. IX. Additional light-curves. Astrophys. J. 135, 906–924.

Grimm, R.E., McSween Jr., H.Y., 1989. Water and the thermal evolution of carbonaceous chondrite parent bodies. Icarus 82, 244–280.

Hapke, B., 1993. Theory of Reflectance and Emittance Spectroscopy. Cambridge Univ. Press, Cambridge, UK.

Hapke, B., 2002. Bidirectional reflectance spectroscopy. 5. The coherent backscatter opposition effect and anisotropic scattering. Icarus 157, 523–534.

Helfenstein, P., Veverka, J., 1989. Physical characterization of asteroid surfaces from photometric analysis. In: Binzel, R.P., Gehrels, T., Matthews, M.S. (Eds.), Asteroids II. Univ. of Arizona Press, Tucson, pp. 557–593.

Helfenstein, P., Hillier, J., Weitz, C., Veverka, J., 1991. Oberon: Color photometry from Voyager and its geological implications. Icarus 90, 14–29.

Helfenstein, P., and 23 colleagues, 1994. Galileo photometry of Asteroid 951 Gaspra. Icarus 107, 37–60.

Helfenstein, P., and 10 colleagues, 1996. Galileo photometry of Asteroid 243 Ida. Icarus 120, 48–65.

Hillier, J., Veverka, J., Helfenstein, P., Lee, P., 1994. Photometric diversity of terrains on Triton. Icarus 109, 296–312.

Johnson, T.V., Fanale, F.P., 1973. Optical properties of carbonaceous chondrites and their relationship to asteroids. J. Geophys. Res. 78, 8507–8518.

King, T.V.V., Clark, R.N., Calvin, W.M., Sherman, D.M., Brown, R.H., 1992. Evidence for ammonium-bearing minerals on Ceres. Science 255, 1551–1553.

Lagerkvist, C.-I., Magnusson, P., 1990. Analysis of asteroid lightcurves. II. phase curves in a generalized HG-system. Astron. Astrophys. Suppl. 86, 119–165.

Lane, A.L., Nelson, R.M., Matson, D.L., 1981. Evidence for sulfur implantation in Europa's UV absorption band. Nature 292, 38–39.

Larson, H.P., Feierberg, M.A., Fink, U., Smith, H.A., 1979. Remote spectroscopic identification of carbonaceous chondrite mineralogies applications to Ceres and Pallas. Icarus 39, 257–271.

Lean, J., VanHoosier, M., Brueckner, G., Prinz, D., Floyd, L., Edlow, K., 1992. SUSIM/UARS observations of the 120–300 nm flux variations of the Sun during the maximum of the solar cycle: Inferences for the 11-year cycle. Geophys. Res. Lett. 19, 2203–2206.

Lebofsky, L.A., Feierberg, M.A., Tokunaga, A.T., Larson, H.P., Johnson, J.R., 1981. The 1.7- to 4.2-micron spectrum of Asteroid 1 Ceres—Evidence for structural water in clay minerals. Icarus 48, 453–459.

Li, J., A'Hearn, M.F., McFadden, L.A., 2004. Photometric analysis of Eros from NEAR data. Icarus 172, 415–431.

McCord, T.B., Sotin, C., 2005. Ceres: Evolution and current state. J. Geophys. Res. 110. E05009.

McEwen, A.S., 1991. Photometric functions for photoclinometry and other applications. Icarus 92, 298–311.

Michalak, G., 2000. Determination of asteroid masses. I. (1) Ceres, (2) Pallas, and (4) Vesta. Astron. Astrophys. 360, 363–374.

Millis, R.L., and 41 colleagues, 1987. The size, shape, density, and albedo of Ceres from its occultation of BD + 8° 471. Icarus 72, 507–518.

Minnaert, M., 1941. The reciprocity principle in lunar photometry. Astrophys. J. 93, 403–410.

Mitchell, D.L., Ostro, S.J., Hudson, R.S., Rosema, K.D., Campbell, D.B., Velez, R., Chandler, J.F., Shapiro, I.I., Giorgini, J.D., Yeomans, D.K., 1996. Radar observations of asteroids 1 Ceres, 2 Pallas, and 4 Vesta. Icarus 124, 113–133.

Murchie, S., and 10 colleagues, 2002. Color variations on Eros from NEAR multispectral imaging. Icarus 155, 145–168.

Noll, K.S., Weaver, H.A., Gonnella, A.M., 1995. The albedo spectrum of Europa from 2200 A to 3300 A. J. Geophys. Res. 100, 19057–19059.

Noll, K.S., Johnson, R.E., Lane, A.L., Domingue, D.L., Weaver, H.A., 1996. Detection of ozone on Ganymede. Science 273, 341–343.

Parker, J.W., Stern, S.A., Thomas, P.C., Festou, M.C., Merline, W.J., Young, E.F., Binzel, R.P., Lebofsky, L.A., 2002. Analysis of the first disk-resolved images of Ceres from ultraviolet observations with the Hubble Space Telescope. Astron. J 123, 549–557.

Pavlovsky, C., and 23 colleagues, 2004. ACS Instrument Handbook, Version 5.0. STScI, Baltimore.

Pavlovsky, C., and 31 colleagues, 2005. ACS Data Handbook, Version 4.0. STScI, Baltimore.

Russell, C.T., and 20 colleagues, 2004. Dawn: A journey in space and time. Planet. Space Sci. 52, 465–489.

Sack, N.J., Johnson, R.E., Boring, J.W., Baragiola, R.A., 1992. The effect of magnetospheric ion bombardment on the reflectance of Europa's surface. Icarus 100, 534–540.

Saint-Pé, O., Combes, M., Rigaut, F., 1993. Ceres surface properties by high-resolution imaging from Earth. Icarus 105, 271–281.

Schober, H.J., 1976. Photoelectric photometry of 1 Ceres during the Ceres-campaign 1975. Mitt. Astron. Ges. 40, 207–210.

Simonelli, D.P., Wisz, M., Switala, A., Adinolfi, D., Veverka, J., Thomas, P.C., Helfenstein, P., 1998. Photometric properties of Phobos surface materials from Viking images. Icarus 131, 52–77.

Soderblom, L.A., Boice, D.C., Britt, D.T., Brown, R.H., Buratti, B.J., Kirk, R.L., Lee, M., Nelson, R.M., Oberst, J., Sandel, B.R., 2004. Imaging Borrelly. Icarus 167, 4–15.

Taylor, R.C., Gehrels, T., Capen, R.C., 1976. Minor planets and related objects. XXI. Photometry of eight asteroids. Astron. J. 81, 778–786.

Tedesco, E.F., 1989. Asteroid magnitudes, UBV colors, and IRAS albedos and diameters. In: Binzel, R.P., Gehrels, T., Matthews, M.S. (Eds.), Asteroids II. Univ. of Arizona Press, Tucson, pp. 1090–1138.

Tedesco, E.F., Taylor, R.C., Drummond, J., Harwood, D., Nickoloff, I., Scaltriti, F., Schober, H.J., Zappala, V., 1983. Worldwide photometry and lightcurve observations of 1 Ceres during the 1975–1976 apparition. Icarus 54, 23–29.

Thomas, P.C., Adinolfi, D., Helfenstein, P., Simonelli, D., Veverka, J., 1996. The surface of Deimos: Contribution of materials and processes to its unique appearance. Icarus 123, 536–556.

Thomas, P.C., Parker, J.W., McFadden, L.A., Russell, C.T., Stern, S.A., Sykes, M.V., Young, E.F., 2005. Differentiation of the Asteroid Ceres as revealed by its shape. Nature 437, 224–226.

Verbiscer, A.J., Veverka, J., 1992. Mimas: Photometric roughness and albedo map. Icarus 99, 63–69.

Verbiscer, A.J., Veverka, J., 1994. A photometric study of Enceladus. Icarus 110, 155–164.

Veverka, J., Helfenstein, P., Skypeck, A., Thomas, P., 1989. Minnaert photometric parameters for the satellites of Uranus. Icarus 78, 14–26.

Viateau, B., Rapaport, M., 1998. The mass of (1) Ceres from its gravitational perturbations on the orbits of 9 asteroids. Astron. Astrophys. 334, 729–735.

Vilas, F., McFadden, L.A., 1992. CCD reflectance spectra of selected asteroids. I. Presentation and data analysis considerations. Icarus 100, 85–94.

Vilas, F., Larson, S.M., Hatch, E.C., Jarvis, K.S., 1993. CCD reflectance spectra of selected asteroids. II. Low-albedo asteroid spectra and data extraction techniques. Icarus 105, 67–78.

Wagner, J.K., Hapke, B.W., Wells, E.N., 1987. Atlas of reflectance spectra of terrestrial, lunar, and meteoritic powders and frosts from 92 to 1800 nm. Icarus 69, 14–28.

Watson, K., Murray, B.C., Brown, H., 1963. The stability of volatiles in the Solar System. Icarus 1, 317–327.

Wilson, L., Keil, K., Browning, L.B., Krot, A.N., Bourcier, W., 1999. Early aqueous alteration, explosive disruption, and re-processing of asteroids. Meteor. Planet. Sci. 34, 541–557.